Available online at www.sciencedirect.com

ScienceDirect

Advances in Space Research 75 (2025) 6140–6157

ADVANCES IN SPACE RESEARCH (a COSPAR publication)

www.elsevier.com/locate/asr

Impact of the antenna characteristics on sea surface parameters estimated from low- and high-resolution satellite altimetry

Christopher Buchhaupt [a,*], Alejandro Egido [b], Salvatore Dinardo [c], Claire Maraldi [d], Thomas Moreau [e], Luciana Fenoglio [f]

[a] Earth System Science Interdisciplinary Center, Cooperative Institute for Satellite Earth System Studies, University of Maryland, 5825 University Research Ct suite 4001, College Park 20740, USA

[b] European Space Research and Technology Centre, European Space Agency, Keplerlaan 1, Noordwijk 2201, Netherlands

[c] European Organisation for the Exploitation of Meteorological Satellites, Eumetsat Aallee 1, Darmstadt 64295, Germany

[d] Centre National d'Etudes Spatiales (CNES), 18. avenue Edouard Belin, Cedex 09, Toulouse 31401, France

[e] Collecte Localisation Satellites (CLS), 11, rue Hermès, Parc Technologique du Canal, Ramonville Saint-Agne 31520, France

[f] Astronomical, Physical and Mathematical Geodesy, University of Bonn, Nußallee 17, Bonn 53115, Germany

Received 13 August 2024; received in revised form 24 February 2025; accepted 26 February 2025
Available online 5 March 2025

Abstract

In this study, we present an extension to existing numerical retrackers of synthetic-aperture radar (SAR) altimetry signals considering a non Gaussian antenna characteristic. To our knowledge at the time of writing, this manuscript presents the most consistent retrieval of geophysical parameters compared to Low Resolution Mode (LRM) retracking results. The novelty is an approximation of the theoretical antenna pattern with a sum of three Gaussian functions to mitigate the sea surface height estimation errors for Sentinel-3A and Sentinel-6A in SAR mode. Additionally, we explain offsets in the derived closed-form equation and describe the mean along-track water velocity u_x (later mean line of sight velocity) as function of eastward and northward wind This allows us to mitigate the effects of u_x in a SAR stack and a lookup table is generated to correct the sea surface height estimates in SAR mode. Further on, we discuss how this new approach performs with respect to different antenna pattern implementations by processing five months (cycles 72 to 76) of Sentinel-3A and six months (cycles 17 to 42) of Sentinel-6A level 1A data on a global scale. We observe that the new retracking method is, on average, more accurate with respect to LRM. To ensure that the results of the new retracker are not biased, we retrack using the new and the current state-of-the-art method on Sentinel-3A and Sentinel-6A data produced in a Monte Carlo simulation. We analyze the simulation results with respect to the accuracy of sea level anomalies as function of the significant wave height (SWH), considering as reference the LRM sea level anomalies. We show that the accuracy of the new antenna characterization is higher compared to a single Gaussian approximation.

Keywords: Delay-Doppler altimetry; Retracking; Sea surface height; Sea state; Directional wind retrieval; Antenna pattern

1. Introduction

For several decades, nadir-looking satellite radar altimeter missions have been routinely used to monitor ocean surface heights and sea state parameters. In a process called retracking, parameterized models for the expected radar power returned from a randomly rough surface are fit to the averages of radar pulse echoes in order to retrieve the parameters known as sea surface height (SSH) and significant wave height (SWH), and the normalized radar cross-section, σ_0, from which wind speed is derived. The

* Corresponding author.
E-mail address: cbuchhau@umd.edu (C. Buchhaupt).

https://doi.org/10.1016/j.asr.2025.02.056
0273-1177/

Nomenclature

CRISTAL Copernicus Polar Ice and Snow Topography Altimeter
DDA delay Doppler altimetry
DDM delay Doppler map
ECMWF European Centre for Medium-Range Weather Forecasts
ERA5 ECMWF Reanalysis v5
ESA European Space Agency
FF-SAR fully focused SAR
FT Fourier transform
LRM Low Resolution Mode
LSA Laboratory for Satellite Altimetry
NOAA National Oceanic and Atmospheric Administration
PDF probability density function
PRF Pulse Repetition Frequency
PTR point target response
SAMOSA SAR Altimetry Mode Studies and Applications over Ocean, Coastal Zones and Inland Water
SAR synthetic-aperture radar
SARAL Satellite with ARgos and ALtiKa
SINC Signal Model involving fast Numerical Convolutions
SINC2 SINC based conventional altimetry retracker
SINCS SINC based unfocused SAR altimetry retracker
SINCS-OV SINC based unfocused SAR altimetry retracker including orbital velocities of wave particles
SIRAL Synthetic Aperture Interferometric Radar Altimeter
SLA Sea Level Anomaly
SNR Signal-to-Noise-Ratio
SSH sea surface height
SWH significant wave height
UF-SAR unfocused SAR
ZSK zero skewness

parameters are associated to an area of ocean surface called the observed footprint.

In the first few decades of altimetry, only incoherent averaging of pulse echoes was used, a technique now called Low Resolution Mode (LRM). The parameterized model for LRM is known as the Brown model (Brown, 1977), and the retracker for LRM is the MLE3/4 retracker (Amarouche et al., 2004), that uses an unweighted least square estimator derived from a maximum likelihood estimator from which 3 or 4 parameters are estimated. The LRM footprint is in a circle of a few km in diameter, and the diameter increases as SWH increases (Chelton et al., 1989).

In the last 14 years, SAR altimeter missions - due to a higher Pulse Repetition Frequency (PRF) - have provided radar echoes that can be coherently processed to narrow the footprint in the direction of spacecraft flights. FF-SAR altimetry (Egido and Smith, 2016) takes aperture synthesis to the maximum limit and can measure water surface heights in rivers and canals that are very narrow (a few meters) in the direction of flight (Kleinherenbrink et al., 2020). However, over the open ocean, the standard practice, known as unfocused SAR (UF-SAR) or Delay/Doppler altimetry (Raney, 1980), synthesizes an aperture for only a few milliseconds of the flight, narrowing the footprint to about 300 m in the flight direction while leaving the across-flight dimension the same size as for LRM altimetry. This standard approach to ocean SAR altimetry is the concern of this paper; here, to distinguish it from LRM altimetry, it is simply called SAR altimetry. While a SAR signal model was first developed by Wingham et al. (2004), the SAMOSA2 retracker (Ray et al., 2015) — named after the project SAR Altimetry Mode Studies and Applications over Ocean, Coastal Zones and Inland Water (SAMOSA) — is the current state-of-the-art algorithm. It is capable of retrieving SSH, SWH, and wind speed from the SAR altimeter return waveform power, which is displayed as a one-dimensional function of two-way travel time.

Geophysical parameters retrieved from SAR altimetry can be more precise than those retrieved from LRM altimetry, but LRM and SAR retrievals may have different accuracies and biases. SAR altimetry exploits Doppler shifts arising from relative motion between the altimeter antenna and the radar scattering points on the sea surface; this may make the SAR parameter estimates sensitive to the direction of ocean surface motions caused by winds and waves. LRM gives equal weight to radar scatterers lying at all azimuths within the circular measurement area; thus, LRM parameter estimates should be independent of any angle between wind or wave propagation and the spacecraft flight direction.

The first generation of SAR altimeters, CryoSat-2 (Wingham et al., 2006) and Sentinel-3 (Donlon et al., 2012), could operate in either LRM or SAR modes, but only by one mode at a time, exclusive of the other mode. Differences in LRM and SAR estimates, if any, had to be found by comparing SAR mode estimates to observations

from so-called pseudo-LRM signals, which mimic LRM, but are computed in SAR mode. In this way, it was found that the CryoSat-2 SAR mode SWH retrievals differed from pseudo-LRM by up to 20 cm. Buchhaupt (2019) showed that the standard deviation of vertical wave-particle velocities σ_v would blur the Doppler spectrum generated in the SAR mode; this would lead to biased SWH estimates because one-dimensional SAR retrackers that are in use would not be able to distinguish between the effect of SWH and the effect of σ_v.

To improve the accuracy of SWH retrievals from SAR altimetry, Buchhaupt (2019) introduced the SINCS-OV (signal model involving numerical convolutions for SAR introducing orbital velocities) retracker, which estimates the geophysical parameters and σ_v by fitting a model to a two-dimensional stack displaying radar echo power as a function of both two-way travel time and Doppler frequency. While this approach mitigated the differences between pseudo-LRM and SAR estimates of SWH, the σ_v estimates did not agree well with observations from buoys and model forecasts from the European Centre for Medium-Range Weather Forecasts (ECMWF). This issue was addressed in Buchhaupt et al. (2023) by considering that the SAR altimeter may be sensitive to vertical wave motion only where wave slopes are close to radar incidence angles, making the observable σ_v smaller than the actual σ_v by a factor a_v, which depends mainly on wave steepness, S_m; correcting σ_v estimates from SINCS-OV for the a_v effect resulted in σ_v values consistent with ECMWF and buoy measurements in the German Bight.

Although the σ_v effect with its a_v correction seemed to solve the problem of the SWH estimation, Raynal et al. (2019) tested the range estimate consistency between SAR and pseudo-LRM for Sentinel-3A by generating range difference maps between both modes and they found anomalies depending on the orbit direction by comparing ascending and descending passes. The geographical distribution of these differences suggested a correlation with the global pattern of the north–south wind speed. In Buchhaupt et al. (2023) this issue could be addressed by introducing a mean line-of-sight velocity u_x causing a scaling of the unfocused SAR stack in the Doppler-frequency domain. Considering u_x as an estimable parameter in the unfocused SAR retracking of Sentinel-6A (Donlon et al., 2021) stacks removes those SSH differences between pseudo-LRM and unfocused SAR. It can be shown that u_x is proportional to the wind-speed and the cosine of the wind-direction with respect to the satellite track.

Otherwise, no additional sea-state effects seem to be necessary to include into an unfocused SAR stack model at this point. However, other sea state effects, such as the geometric effects from long ocean waves, also have an impact on SAR-mode data but are not currently accounted for in the processing (Moreau et al., 2018; Rieu et al., 2021). These effects violate the assumptions of sea surface homogeneity within the altimeter footprint considered in retracking models and therefore need to be addressed outside of retracking, more likely in post-processing. Mean wave-steepness and mean square slope are, on the other hand, already considered. The latter by assuming that wave slope standard deviations are much bigger than the incidence angle. On the other hand, the mean wave-steepness is assumed to be constant such that the wave elevation displacement skewness equals 0.1. This is probable not true for low and very high sea states and is planned to be addressed in another study. In this work we prioritize the antenna pattern, which was for the first time investigated thoroughly in Dinardo et al. (2022), over those issues. The reason behind this decision is that we assume - based on results presented in Dinardo et al. (2022) - that the non Gaussian antenna pattern might cause bigger errors than the other issues mentioned before. One major conclusion of Dinardo et al. (2022) is that the antenna pattern does not perfectly follow a Gaussian as proposed by Brown (1975) but more a Bessel-like pattern as shown in Fig. 1 showing errors of up to -2 dB for a Gaussian antenna pattern while with a Bessel pattern only up to -0.25 dB are observable within given elevation angles. In this study we give an overview about how the antenna pattern affects the retracking of results of pseudo-LRM and unfocused SAR. In Section 2 we discuss a more realistic antenna pattern and how it can be introduced in a altimetry signal model. In Section 3 and 4 we utilize numerical simulations to provide an overview about potential retracking errors caused by a Gaussian antenna pattern and if the approach presented in this study is suitable to mitigate those errors. In Section 5 we present results from a real data processing campaign to discuss retracking results improvements achievable with the approach presented in this study. Finally, we conclude and summarize our findings in Section 6.

2. Antenna Pattern

According to Dinardo et al. (2022) the antenna pattern of a radar altimeter can be described as a combination of a uniform circular or elliptical aperture and a tapered circular or elliptical aperture. The resulting one-way antenna gain function can be described as (Dinardo et al., 2022; Stutzman and Thiele, 2012):

$$G(x,y) = G_0 \left[\frac{C \cdot f(x,y,0) + \frac{1-C}{n+1} \cdot f(x,y,n)}{C + \frac{1-C}{n+1}} \right]^2 \tag{1}$$

in which G_0 is the nominal antenna gain, $n$describes the tapering coefficient and $C$the pedestal coefficient describing a nonzero illumination at the antenna edge. A tapering coefficient of $n = 0$ describes an uniform electrical field distribution, $n = 1$ a parabolic taper, and $n = 2$ a parabolic square taper (see Table 8–1 in Stutzman and Thiele (2012)). $f(x,y,n)$ gives the antenna pattern, which is given

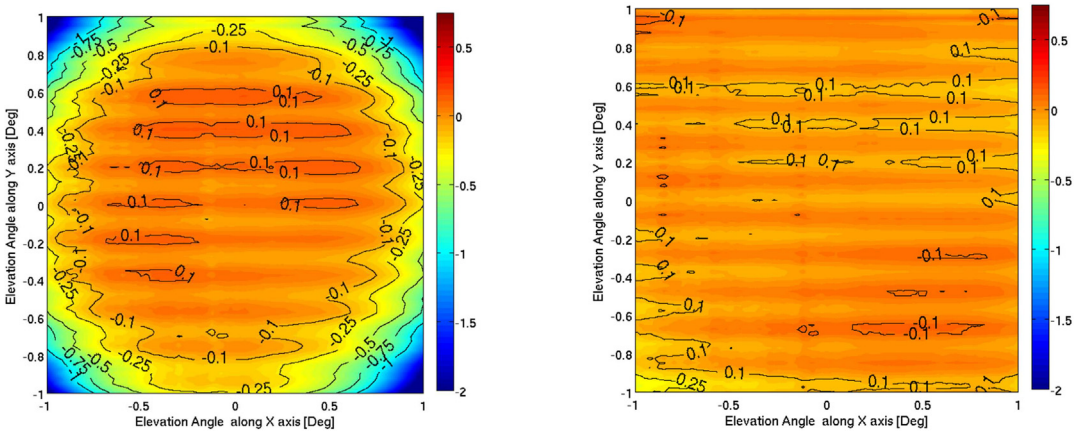

Fig. 1. Sentinel-6MF POSEIDON4 Ku-band power radiation pattern differences given in decibel between real antenna pattern and Gaussian pattern model (left) and difference between Bessel pattern model and real pattern (right). Both Gaussian and Bessel patterns have been computed for antenna beamwidths of 1.34 degree and 1.32 degree, respectively, along the roll and pitch axis. Source: Fig. 3 from Dinardo et al. (2022).

by a zero order Hankel transform $\mathscr{H}_0$ of the aperture electrical field distribution given by Dinardo et al. (2022, 2012):

$$f(x,y,n) = 2^{n+1}(n+1)!\,\frac{J_{n+1}(\mu)}{\mu^{n+1}} \tag{2}$$

in which $J_{n+1}(x)$ is the Bessel function of first kind of order $n+1$, and μ a variable defined as

$$\mu = \sqrt{\beta_x^2\left(\frac{x-x_p}{h_s}\right)^2 + \beta_y^2\left(\frac{y-y_p}{h_s}\right)^2} \tag{3}$$

with $\beta_x = \frac{\pi k_{sh}}{\theta_{3dBx}}, \beta_y = \frac{\pi k_{sh}}{\theta_{3dBy}}, x_p = h_s \tan\xi_p$, and $y_p = h_s \tan\xi_r$. θ_{3dBx} is the half power beamwidth in along-track (or pitch) dimension and θ_{3dBy} is the half power beamwidth in across-track (or roll) dimension. Additionally, h_s is the satellite orbit altitude with respect to the reference surface, ξ_p the pitch mispointing angle, and ξ_r the roll mispointing angle. k_{sh} is an auxiliary variable to ensure that the antenna gain function equals 0.5 at the half power beam-width. Table 1 gives k_{sh} values for tapering coefficients used in this study.

Since an implementation of the antenna gain function as described in Eq. 1 is difficult we approximate the squared antenna gain function by a sum of three Gaussian:

$$G(x,y)^2 \approx G_0^2 \sum_{i=1}^{3} \Delta G_i^2 \exp\left\{-2a_i^2\left(\frac{x-x_p}{h_s}\right)^2 - 2b_i^2\left(\frac{y-y_p}{h_s}\right)^2\right\} \tag{4}$$

with $a_i = \frac{\sqrt{ln(2)\Delta\theta_i}}{\sin(\theta_{3dBx}/2)}$ and $b_i = \frac{\sqrt{ln(2)\Delta\theta_i}}{\sin(\theta_{3dBy}/2)}$. ΔG_i^2 describes a factor and $\Delta\theta_i$ a scaling. Three terms were chosen as for four terms or more the fitting errors did not improve enough to justify the additional computation costs.

The implementation of the sum of three Gaussian is simple as all physical retracker already have a solution for a single Gaussian implemented. Therefore, the sum of three Gaussian approximation for the antenna gain function results into the sum of three delay Doppler maps (DDMs) for SAR or the sum of three waveforms for LRM. Another benefit of the sum of three Gaussian approximation is that it can be implemented into a numerical retracker with only a few additional calculations. This is possible because a numerical retracker calculates the power of a SAR signal in the slow-time/frequency domain as

$$\hat{\hat{P}}_{DA}(f,t_s) = \widehat{\widehat{FSSR}}_{DA}(f,t_s) \cdot \widehat{\widehat{PDF}}(f,t_s) \cdot \widehat{\widehat{PTR}}(f,t_s) \tag{5}$$

with the double hats describing that a two dimensional Fourier transform (FT) was performed to the term, a single hat denotes a one dimensional FT from time-delay to frequency, $FSSR_{DA}$ the flat sea surface response, $PDF$the joint probability density function of vertical wave particle velocities and wave elevation displacement, and $PTR$the return of a point target. For LRM the power is according to Buchhaupt et al. (2018) given as a special case of the SAR notation:

$$\hat{P}_{CA}(f) = \widehat{\widehat{FSSR}}_{DA}(f,0) \cdot \widehat{\widehat{PDF}}(f,0) \cdot \widehat{\widehat{PTR}}(f,0) \tag{6}$$

The $\widehat{\widehat{FSSR}}_{DA}$ or $\widehat{\widehat{FSSR}}_{CA}$ and $\widehat{\widehat{PTR}}$ do not depend on any considered geophysical parameters and therefore they can be computed outside of the Levenberg–Marquardt algorithm. Therefore, it is sufficient to apply the sum of three Gaussian only once per 20 Hz surface location or even less often. For analytical retracker such as SAMOSA2 it would be necessary to calculate the whole DDM three times (once for each Gaussian) per function evaluation within the Levenberg–Marquardt algorithm.

Table 1
k_{sh}values for different tapering coefficients $n$and pedestal coefficient $C = 0$.

n	k_{sh}
0	1.028993969962192
1	1.269685553346112
2	1.472712212127717

Table 2
Sum of three Gaussians antenna pattern power coefficients for different tapering coefficients $n$and pedestal coefficient $C = 0$.

n	0	1	2
ΔG_1^2	−0.514536354097967	−0.517055781632939	−0.518308050610166
ΔG_2^2	+1.877670720299080	+1.877223856777140	+1.876731294335370
ΔG_3^2	−0.363274928545989	−0.360249726481299	−0.358473244101736

As according to Dinardo et al. (2022) the pedestal coefficient $C$is usually set to zero in this study the case $C \neq 0$ is not considered. Table 2 gives the coefficients ΔG_i^2, and Table 3 $\Delta\theta_i$. Both were derived by fitting the analytical realization from Eq. 1 with a sum of three Gaussians as in Eq. 4 using a global multi-start based least-squares estimator.

Table 2 shows the power coefficients for different taper coefficients. It can be observed that some coefficients are negative, which implies that the sum of three Gaussians approximation allows negative power values. However, only in the sidelobes which are in most cases not observable by a nadir looking instrument such as a radar altimeter as those fall outside the range receiving window. The coefficents presented in Table 3 gives the width scaling coefficients of the sum of three Gaussians approximation. While the width scaling parameters for the positive power scaling are about one, the coefficients corresponding to negative power factors are either higher or lower than one.

The accuracy of this approximation is shown in Fig. 2 for squared antenna gain functions normalized to one. As shown in Fig. 2 within the range of $\pm 1.5\theta_{3dBx}$ and $\pm 1.5\theta_{3dBy}$ a Gaussian squared antenna gain function fits the Bessel like squared antenna gain function with an error of less than $12E-3$. It is worth mentioning that with increasing tapering coefficient the error becomes smaller. In comparison, the sum of three Gaussian approximates the squared antenna gain function better with an error of less than $2E-04$ for incidence angles below the half-power beamwidth. Even at higher incidence angles up to 1.5 times the half power beamwidth the sum of three Gaussians gives a five times lower error.

3. Simulation of radar altimetry signals

In order to test and validate our findings presented in the previous sections, we perform numerical simulations of radar altimetry signals using the Bessel-like antenna gain function presented in Eq. 1.

Table 3
Sum of three Gaussians antenna pattern width coefficients for different tapering coefficients $n$and pedestal coefficient $C = 0$.

n	0	1	2
$\Delta\theta_1$	1.286493692597880	1.244826105696910	1.216476574490750
$\Delta\theta_2$	0.979601075196802	0.985508262559527	0.988832349619966
$\Delta\theta_3$	0.655404322621908	0.698391528915493	0.728621361997738

This is achieved by defining an observed impulse response function $Q(\mu,\sigma,T)$ describing the convolution of a squared sine cardinal with bandwidth $2T$ and a probability density function (PDF) of a normally distributed random variable with zero mean and standard deviation σ, given as

$$Q(\mu,\sigma,T) = \int_{-\infty}^{\infty} \frac{1}{\sqrt{2\pi\sigma^2}} \exp\left\{-\frac{(\mu-\mu\prime)}{2\sigma^2}\right\} \frac{\sin(\pi\mu\prime T)^2}{(\pi\mu\prime T)^2} d\mu\prime \tag{7}$$

An analytical expression can be found with Dawson functions $F(z) = e^{-z^2}\int_0^z e^{u^2}dy$. For $\sigma > 0$ $Q(\mu,\sigma,T)$ can be written as

$$\begin{aligned} Q(\mu,\sigma,T) = {} & \frac{\exp\left\{-2\pi^2\sigma^2T^2\right\}\cos(2\pi T\mu)-1}{2\pi^2\sigma^2T} + \frac{z_r F(z_r)}{\pi^2\sigma^2T} \\ & + \frac{\exp\left\{-2\pi^2\sigma^2T^2\right\}}{\pi^2\sigma^2T} \Re\{\exp\{2\pi i T\mu\} z F(z)\} \end{aligned} \tag{8}$$

$$z = \frac{\mu}{\sqrt{2}\sigma} + \sqrt{2}\pi i\sigma T = z_r + i z_i \tag{9}$$

with $\Re\{z\}$ the real part, z_r the real part and z_i the imaginary part of the auxiliary variable z, and $i = \sqrt{-1}$ the imaginary unit.

A numerical solution for the two-dimensional power function observed by a delay Doppler altimetry (DDA) at given Doppler frequencies f_D and range delays τ_r can then be calculated by integrating over an equidistant surface grid applying the mid-point rule:

$$\begin{aligned} P_{DA}(\tau_r, f_D) = {} & \sum_{k=0}^{K-1} Q(f_D - f_k, \sigma_t, \tau_b) \\ & \times \sum_{l=0}^{L-1} G(x_k, y_l)^2 \, Q\left(\tau_r - \tau_{kl}, \sigma_s, \tau_p\right) \Delta x \, \Delta y \end{aligned} \tag{10}$$

$$P_{CA}(\tau_r) = \sum_{k=0}^{K-1}\sum_{l=0}^{L-1} G(x_k, y_l)^2 \, Q\left(\tau_r - \tau_{kl}, \sigma_s, \tau_p\right) \Delta x \, \Delta y \tag{11}$$

in which τ_b describes the burst duration, and τ_p is the usable pulse duration. In this study $x_k = -20{,}000m + k\,\Delta x, y_l = -20{,}000m + l\,\Delta y$, $\Delta x = \Delta y = 10m$, $K = L = 4001, \sigma_s = \frac{2}{c}\sigma_z, \sigma_t = a_v\frac{2}{\lambda_c}\sigma_v$, while λ_c is the carrier wavelength of the emitted signal. σ_z is the standard deviation of wave elevation displacements or a quarter of the SWH, σ_v the standard deviation of vertical wave particle velocities, and a_v an attenuation factor considering that only vertical wave particle velocities are observable if the

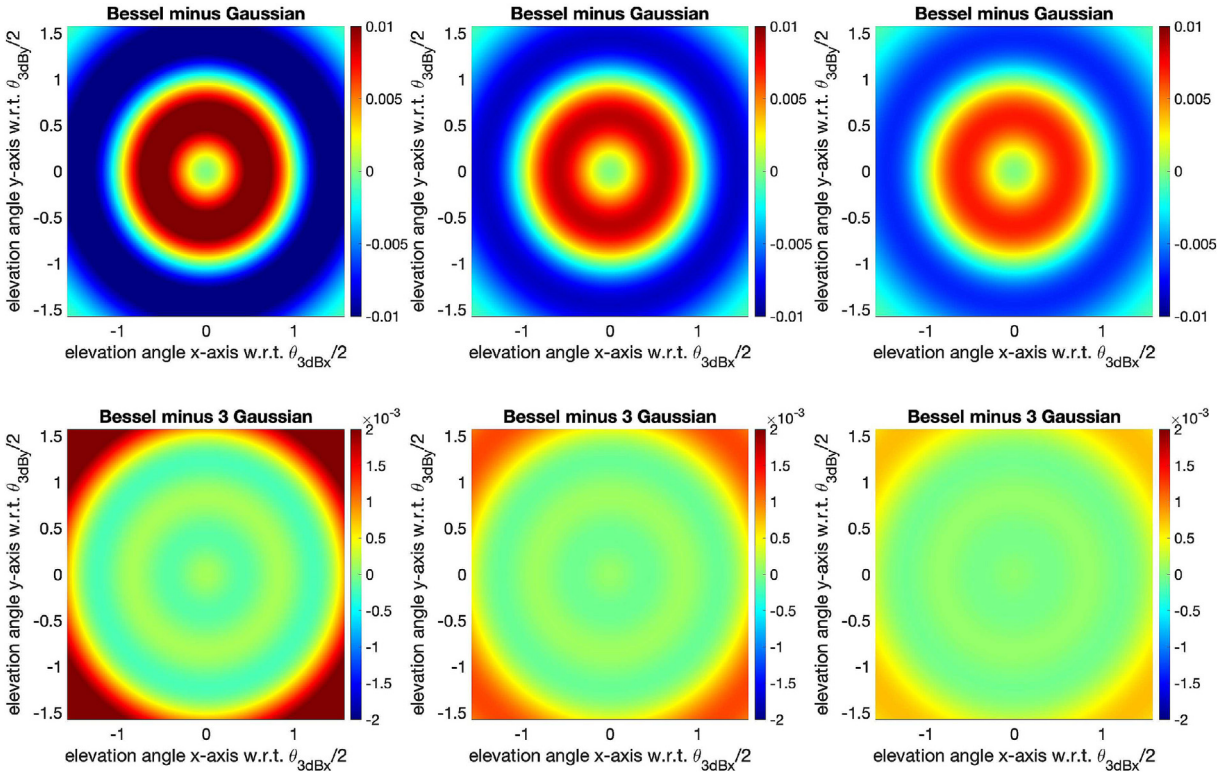

Fig. 2. Squared Bessel like antenna pattern minus Gaussian antenna pattern (upper half) or minus the sum of three Gaussian pattern (lower half). The left column compares the patterns for $n = 0$, the middle one for $n = 1$, and the right one for $n = 2$.

wave slope is very close to the incidence angle of the electromagnetic signal emitted by the radar altimeter.

$$f_k = \frac{2}{\lambda_c}\alpha_x(v_x + u_x)\frac{x_k}{h_s} \tag{12}$$

$$\tau_{kl} = \frac{2}{c}\sqrt{h_s^2 + \alpha_x(x_k^2 + y_l^2)} - \frac{2h_s}{c} \tag{13}$$

in which $\alpha_x = 1 + h_s\kappa_x$ is the along-track curvature coefficient with κ_x the along-track surface curvature, and v_x the along-track velocity of the nadir.

u_x describes a mean line of sight velocity defined in Buchhaupt et al. (2023). It is defined as

$$u_x = \frac{\rho_{xt} - \rho_{yt}\rho_{xy}}{1 - \rho_{xy}^2}\frac{\sigma_v}{\sigma_x} - c_x \tag{14}$$

where c_x is the along-track current velocity plus the along-track Stokes drift, ρ_{xt} is the correlation coefficient between along-track wave slopes and vertical wave-particle velocities, ρ_{yt} is the correlation coefficient between across-track wave slopes and vertical wave-particle velocities, ρ_{xy} is the correlation coefficient between along-track and across-track wave slopes, and σ_x the standard deviations of slope in along-track direction.

The Doppler frequencies for the simulations are chosen to match those of processed signals in a L1B stack product. Therefore $N_p O_x$ equidistant Doppler frequency samples with a step size of $\Delta f_D = \frac{f_p}{N_p O_x}$ and a start value of $f_{D,0} = -\frac{f_p}{2} + \Delta f_D$ are considered. N_p is the number of transmitted pulses per burst, f_p the PRF, and O_x an oversampling factor to mitigate the aliasing caused by the power detection. For the time delay $N_s O_t$ equidistant samples with a step size of $\Delta\tau_r = \frac{1}{O_t f_s}$ and a start value of $\tau_{D,0} = 0ns$ are considered. N_s is the number of considered samples per pulse, f_s the sample frequency, and O_t an oversampling factor to mitigate the aliasing caused by the power detection. Table 4 gives the mission parameter used in the simulation and the retracking. The widening and oversampling parameters used for the simulation and retracking are presented in Table 5. N_x and N_t are parameters - provided for the sake of completeness - used when calculating the numerical signal model to avoid aliasing (Buchhaupt, 2019). They are not necessary to simulate the signals. As simulating can be very time-consuming if all possible parameter combinations are considered, some restrictions need to be set first to reduce the workload.

1. The observed surface is only affected by wind waves, ensuring that no currents or swell effects are considered.
2. The local wave field is fully developed, which means that it can be described by a Pierson–Moskowitz spectrum (Pierson and Moskowitz, 1964).
3. Potential atmospheric refraction effects are not considered.

Table 4
Summary of Sentinel-3A and Sentinel-6A mission parameters used to simulate the DDMs. It is important to note that the pulse repetition frequency is not constant for Sentinel-6A. The f_p value given here is a proxy used when simulating signals.

Symbol	Description	Sentinel-3A	Sentinel-6A
θ_{3dBx}	Along-track half-power beamwidth	1.34°	1.34°
θ_{3dBy}	Across-track half-power beamwidth	1.34°	1.34°
H_N	Nominal orbit altitude	814.5 km	1340 km
s	Negative chirp slope	7.1438 MHz/µs	9.9748 MHz/µs
f_c	Central frequency	13.575 GHz	13.575 GHz
f_p	Pulse-repetition frequency	17825.3 Hz	9100.2 Hz
f_s	Time-delay sample frequency	320 MHz	395 MHz
B	Usable pulse bandwidth	320 MHz	320 MHz
N_b	Number of bursts per radar cycle	4	7
N_s	Number of samples per echo	128	128
N_p	Number of pulses per burst	64	64
C	antenna pedestal coefficient	0	0
n	antenna tapering coefficient	2	2

Table 5
Sampling and window-widening parameters used in calculating the modeled Sentinel-3A or Sentinel-6A DDM.

Symbol	Description	Sentinel-3A	Sentinel-6A
O_t	Time delay oversampling factor	2	2
N_t	Time delay window-widening factor	8	16
O_x	Azimuth oversampling factor	2	2
N_x	Azimuth window-widening factor	2	2

Table 6
Summary of retrackers used in this study.

Retracker	Mode	Input	Estimated Parameter
SINC2	LRM	waveform	A, t_0, σ_z
SINCS-OV2	SAR	stack	$A, t_0, \sigma_z, \sigma_v, u_x$

Using these restrictions to describe U_{10}, σ_v, and u_x in terms of SWH H_s yields the following:

$$U_{10} = 2.1375\sqrt{gH_s} \tag{15a}$$

$$\sigma_v = \sqrt{\mu g\ \sigma_z} \tag{15b}$$

$$u_x \propto \sqrt{U_{10}}\cos\varphi_w \tag{15c}$$

where U_{10} describes the total wind speed ten meters above sea level, $g$the gravity acceleration, and φ_w the wave direction with respect to the satellite track. Eq. 15a results from restrictions 1 and 2, leading to a wave field described by the Pierson–Moskowitz spectrum, Eq. 15b, from the definition of the short-wave non-linearity coefficient μ (Tayfun, 1986), Eq. 15c follows the findings from Buchhaupt et al. (2023) by fitting measured u_x values from Sentinel-6A SAR signals in terms of U_{10}.

In this study, $H_s = \{1\text{mm}, 50\text{cm}, 1\text{m}, 2\text{m}, 6\text{m}, 10\text{m}\}$, a short-wave non-linearity coefficient of $\mu = 0.0546$, an elevation displacement skewness of 0.1, a mean gravity acceleration of $g = 9.81$ m/s, an attenuation factor of $a_v = 0.8$, and wind directions with respect to the satellite flight path of $\varphi_w = \{0.0^\circ, 45.0^\circ, \ldots 180.0^\circ\}$ are used to simulate the signals (negative values for φ_w are not shown here as u_x is symmetric with respect to φ_w (see Eq. (15c))).

Table 6 presents an overview of the retrackers considered in this study. The abbreviation SINC stands for the signal model involving numerical convolutions. SINC2 was the first of the developed numerical retrackers and the name incorporating the point target response (PTR) follows a squared sine cardinal function. The S in SINCS stands for SAR. OV means orbital velocity as it introduces a parameter based on the vertical component of orbital wave motions. In this study, we introduce another parameter, which mostly depends on the mean line-of-sight motions, or in other words, vertical wave-particle velocities, at a given wave slope; thus, we decided to name the new retracker SINCS-OV2, indicating two parameters that are mainly based on orbital velocities. It is important to note that all retrackers accommodate possible negative σ_z and σ_v values - caused by noise - by setting $\sigma_z^2 \mapsto \sigma_z|\sigma_z|$ and $\sigma_v^2 \mapsto \sigma_v|\sigma_v|$. Additionally, retrackers using input signals transformed with the zero skewness (ZSK) approach (Buchhaupt, 2019, Eq. 7.1) estimate the thermal noise t_n as well. Step by step instructions and discussion about how we numerically simulate the signals is given in A.

4. Evaluating the Impact of the Antenna Pattern on Sea State Parameters

To evaluate the impact of the antenna pattern on geophysical parameters three datasets are generated.

- gauss/gauss: Gaussian antenna pattern in the simulation and the retracking.
- jinc/gauss: Antenna pattern according to Eq. 1 in the simulation and a single Gaussian antenna pattern in the retracking.

- jinc/3gauss: Antenna pattern according to Eq. 1 in the simulation and a sum of three Gaussian approximation antenna pattern in the retracking.

The gauss/gauss dataset serves as a reference. In theory it should be bias free for all retracker and parameters, but if an error was made in the implementation of the simulator, or the model used in the retracking is not good enough, or the statistical model is insufficiently described then biases will occur. On the other hand the jinc/gauss dataset is what is actually implemented in operational altimetry processors. Therefore, biases shown in this dataset should show in operational datasets as well. The jinc/3gauss dataset shall then deliver an almost bias free dataset again as it approximates the real antenna pattern. In the following "meas" stands for measured value meaning that it got derived from the retracking output, while real is the value used as a simulation input.

4.1. Sentinel-3A

For Sentinel-3A the simulation and the retracking is performed with the same antenna and orbit parameters. Fig. 3 presents the simulation results including the ZSK transform. The jinc/gauss dataset shows a significant SWH trend for range estimates of about 0.275% SWH, but the bias at two meter SWH is with nine millimeter significant. The datasets using matching antenna patterns in the simulation and retracking are almost bias free for SWHs of two meter or higher and even for lower sea states the range offsets are significantly improved compared to the jinc/gauss dataset. The SWH biases are small for gauss/gauss and jinc/3gauss and even for jinc/gauss they are below five centimeter for SWHs of more than one meter. As a conclusion it can be stated that the ZSK transform in combination with the sum of three Gaussian approximation gives the best results for pseudo-LRM waveform retracking.

For the Sentinel-3A SAR stack retracking the gauss/gauss and jinc/3gauss datasets shown in Fig. 4 are mostly bias free besides a few centimeter per seconds offset for σ_v. This indicates that the retracker model and the simulation match together, even so the simulation used Bessel like antenna pattern and the retracker a sum of three Gaussian as an approximation. The σ_v offsets can be explained by the small number (four) of stacks used when computing the input stack for the retracker. On the other hand, the jinc/gauss datasets shows a 0.19% SWH range trend, a small SWH slope of up to two centimeter, a minor σ_v slope, and a big u_x error of −30% SWH in meter per seconds. Therefore, mostly the range and u_x are affected by the antenna pattern.

As in this study we compare SAR with pseudo-LRM results, we additionally computed the Sea Level Anomaly (SLA) difference between SINCS-OV2 ZSK and SINC2 ZSK. The same will be performed using the real campaign described in Section 5. Fig. 5 shows that the gauss/gauss and jinc/3gauss SLAs differences are below one millimeter for SWHs of more than two meter. For lower values they increase to up to eight millimeters. This can be explained by the lower Signal-to-Noise-Ratio (SNR) of the pseudo-LRM waveforms at low sea states (Walsh, 1982). If the wrong antenna pattern is used a six millimeter offset can be observed at SWH of two meter and a trend of 0.08% SWH can be seen. SWH differences are small enough to be neglected.

4.2. Sentinel-6A

For Sentinel-6A we use a different approach compared to Sentinel-3A. The reason behind is that the official pro-

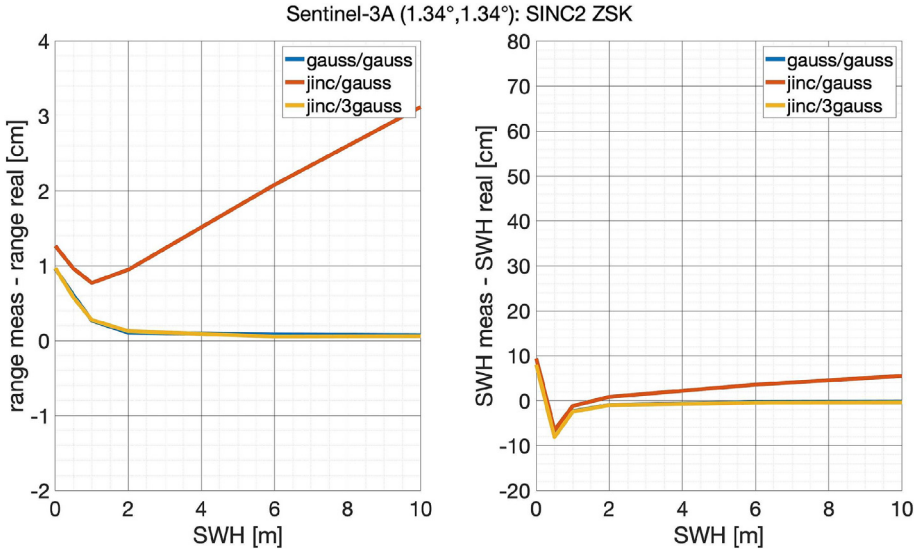

Fig. 3. Sentinel-3A mean pseudo-LRM waveform retracking biases derived by retracking numerically simulated signals with the SINC2 ZSK retracker. Left: Range. Right: SWH.

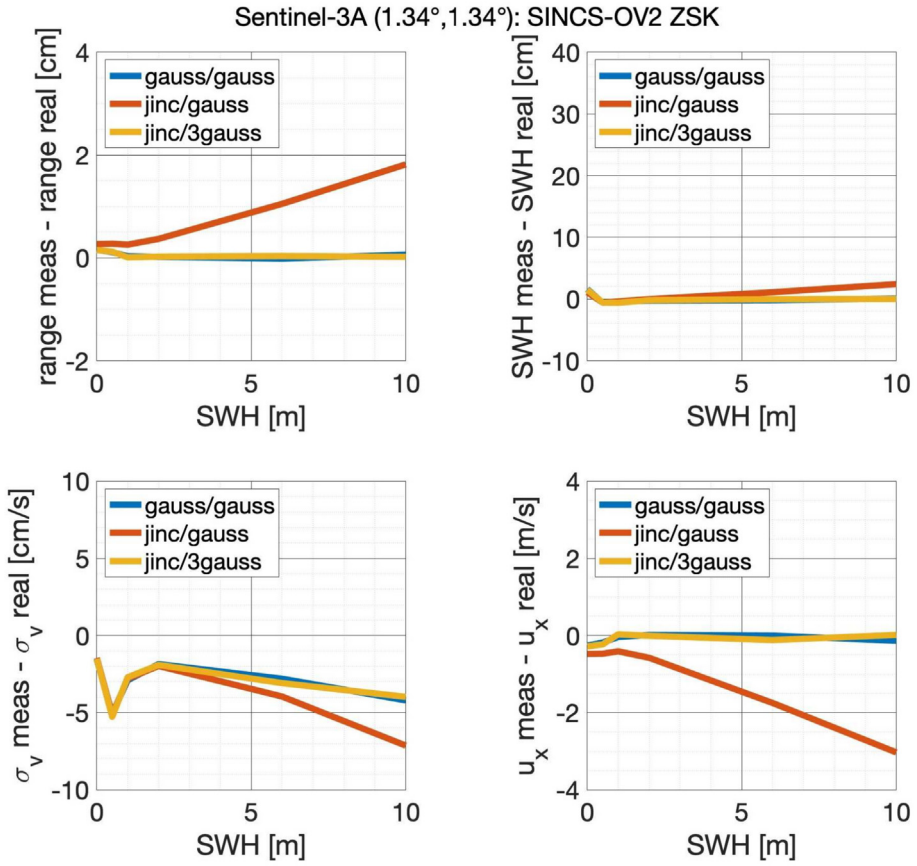

Fig. 4. Sentinel-3A mean SAR stack retracking biases derived by retracking numerically simulated signals with the SINCS-OV2 ZSK retracker. Top left: Range. Top right: SWH. Bottom left: σ_v. Bottom right: u_x.

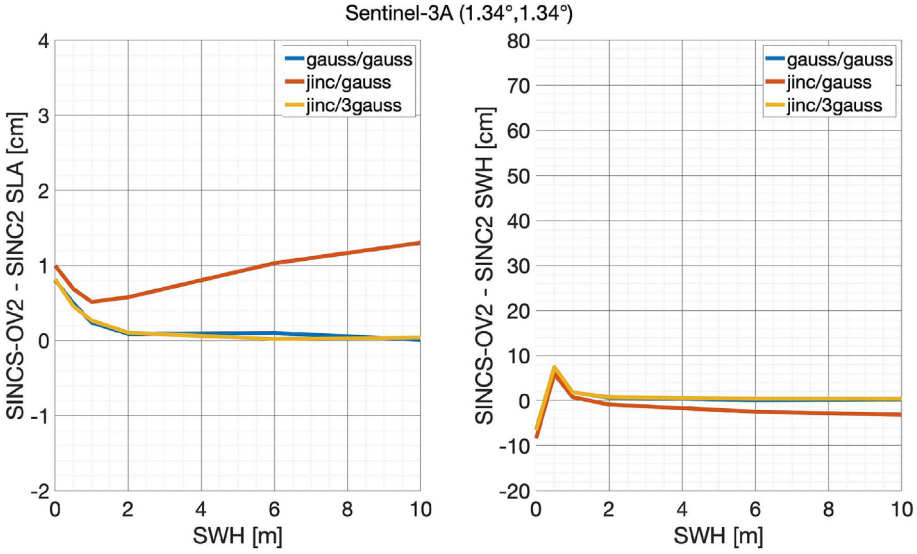

Fig. 5. Sentinel-3A mean retracking difference between SINCS-OV2 ZSK and SINC2 ZSK. Left: SLA. Right: SWH.

duct uses in the L2 processing an along-track half power antenna beam width of 1.34°. However, in Dinardo et al. (2022) it is mentioned that - according to post environmental antenna test measurements - the value providing the best fit with a Bessel like antenna pattern is 1.32°. We asked the European Space Agency (ESA) to get access to those measurements and thankfully we were provided with the antenna frequency cuts for Sentinel-6A. In our analysis we came up with a value of 1.315°as a best fit, which is within rounding precision to the value found in Dinardo

et al. (2022). Therefore, in this study we simulate the signals with $\theta_{3dBx} = 1.315^\circ$, but retrack those with $\theta_{3dBx} = 1.34^\circ$ to mimic the error in the official product. The across-track half power antenna beam width we found is in line with the value reported in the official product and Dinardo et al. (2022) of $\theta_{3dBy} = 1.34^\circ$. Additionally, in Buchhaupt et al. (2023) the official value was used in the retracking campaign as well and we want to keep the results comparable. But this also means that the gauss/gauss and jinc/3-gauss datasets are no longer expected to be bias free even if the stochastic model is correct.

This can be observed in Fig. 6 showing the pseudo-LRM waveform retracking results. The gauss/gauss and jinc/3-gauss datasets show not only the few millimeter range offset but also a −0.175% SWH slope. On the other hand the range slope is 0.038% SWH and an offset of five millimeter for the jinc/gauss dataset, which means that using the wrong along-track half power beam width reduces the errors in range and SWH as shown in the right plot of Fig. 6. If identical θ_{3dBx} values would have been used in the simulation and retracking the results would be comparable with Sentinel-3A, but with lower biases caused by the stochastic model since Sentinel-6A uses $N_b = 7$ bursts in the 20 Hz L1B processing while Sentinel-3A uses four.

The SAR waveform retracking is mostly affected by vertical wave motion effects and not significantly by the antenna pattern. Therefore, we won't discuss this approach for Sentinel-6A again. More interesting are the stack retracking results shown in Fig. 7. For SINCS-OV2 ZSK the range slopes are 0.06% SWH for jinc/gauss. However, for gauss/gauss and jinc/3gauss the slope is smaller with −0.07% SWH. SWH and σ_v results do not show significant offsets or slopes for all datasets. The SWH offsets are even lower than those from Sentinel-3A, which can be explained by the fact that the number of independent bursts used when computing the input stack is with $N_b = 7$ almost twice as big compared to Sentinel-3A leading to a better SNR of the retracked stack. An interesting result is that the u_x biases for the jinc/gauss dataset are with 12% SWH in meters per seconds smaller than those of the gauss/gauss or jinc/3gauss dataset with 37.5% SWH in meters per second. The signs are different compared to Sentinel-3A. Overall, using the wrong along-track antenna pattern seem to have a positive effect if a Gaussian approximation is used in the retracking. In Buchhaupt et al. (2023, Fig. 8) a similar u_x offset pattern as given in Fig. 7 was observed, which indicates that indeed a wrong antenna pattern function in combination with a wrong along-track antenna beam width was apparent. This hypothesis will be tested in the next section where we show u_x offsets for Sentinel-3A and Sentinel-6A.

Fig. 8 shows the differences between SINCS-OV2 ZSK and SINC2 ZSK. One interesting result is that SAR stack and pseudo-LRM waveform SLA estimates are - with a mean difference of a millimeter - very consistent at SWHs of one meter or higher if a Gaussian antenna pattern is with an along-track half power beam width of $\theta_{3dBx} = 1.34^\circ$ is used when retracking a Bessel like antenna pattern with $\theta_{3dBx} = 1.315^\circ$. However, that does not mean that the results are correct. It just means that the antenna pattern used masked those errors out.

5. Global Sentinel-3A and Sentinel-6A Data Investigation

While the simulations give a good first overview about potential errors caused by using antenna characteristics within the retracking not matching the real instrument, it needs to be shown that this issue can be observed within a real data processing campaign.

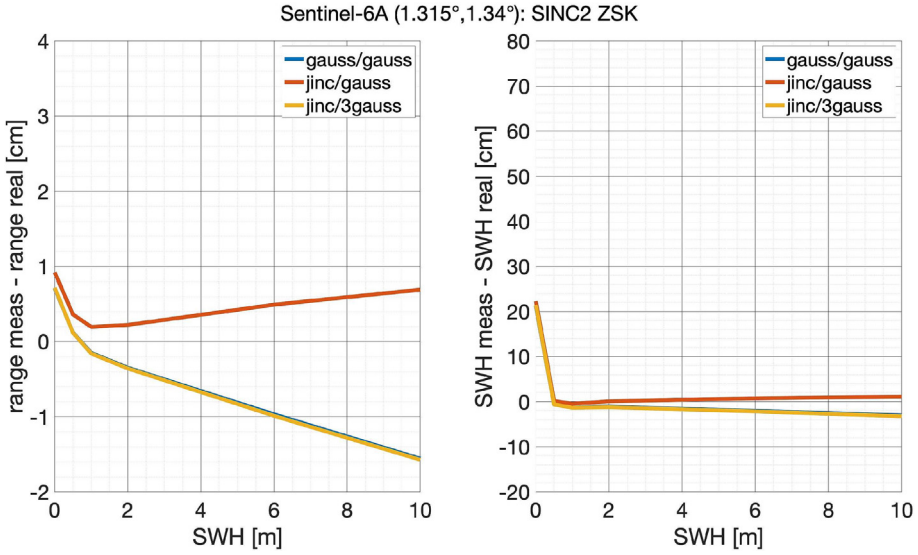

Fig. 6. Sentinel-6A mean pseudo-LRM waveform retracking biases derived by retracking numerically simulated signals with the SINC2 ZSK retracker. Left: Range. Right: SWH.

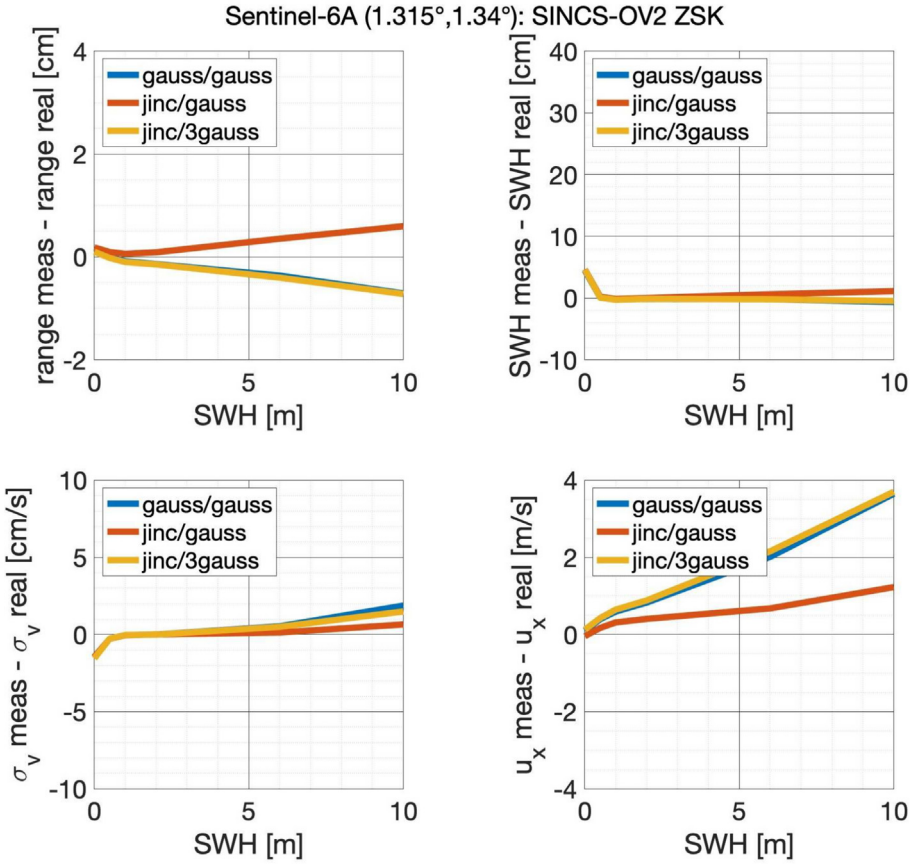

Fig. 7. Sentinel-36A mean SAR stack retracking biases derived by retracking numerically simulated signals with the SINCS-OV2 ZSK retracker. Top left: Range. Top right: SWH. Bottom left: σ_v. Bottom right: u_x.

The SAR stacks were produced using the scientific LSAR-v1.4 L1A to L2 processor - being the experimental in–house processor of the Laboratory for Satellite Altimetry (LSA) - by means of an unfocused SAR processing approach, including the so-called range walk correction (Scagliola et al., 2021) via a chirp Z-transform. Additionally, LSAR attempts to reduce the size of the resulting DDMs by using a non-exact beam-steering approach, which results in $O_x N_p$ Doppler beams with equidistant Doppler frequencies per 20-Hz surface location. N_p is the number of pulses per burst and O_x is the along-track oversampling factor. Since each radar cycle consists of N_b bursts for each surface location and Doppler frequency, N_b Doppler beams occur. Since these will not provide further spatial information about the sea surface, they are averaged to one Doppler beam, resulting in an improved SNR by a factor of $\sqrt{N_b}$ assuming uncorrelated bursts (Egido et al., 2021). It is important to note that the ZSK transform is performed before averaging the N_b Doppler beams as it only works on exponentially distributed data, and after averaging, the samples would adhere to a Gamma distribution. Another difference of LSAR-v1.4 compared to the version used in Buchhaupt et al. (2023) is that antenna amplitude and phase distortion corrections - provided to us by the ESA - were corrected in the L1B processing.

During the L1B to L2 process - usually referred to as retracking - the computation of the model DDMs is performed following Buchhaupt (2019, Section 3.3) or Buchhaupt et al. (2023, Section 5 and Appendix A-C). While for Sentinel-3A the instrument parameters given in Table 4 were used in the retracking for Sentinel-6A the along-track antenna half power beam width is set to $\theta_{3dBx} = 1.315^\circ$ to consider our findings from investigating the post environmental antenna test measurements provided by the ESA.

In this study we focus on the parameters SLA and u_x as those are mostly affected by the antenna pattern. For u_x we use the same approach as in Buchhaupt et al. (2023), which are briefly outlined here. We binned estimated 1-Hz u_x values from SINCS-OV2 ZSK retracking for different ECMWF Reanalysis v5 (ERA5) wind speeds and directions with respect to the satellite track. For wind-speed U_{10}, central values from 0.5 m/s to 15.5 m/s with a step size of 1 m/s were chosen. For wind direction, central values ranged from -175° to 175°, with a step size of 10°. An u_x value is then assigned to the nearest corresponding wind speed and wind direction. From our observations, as u_x closely follows a normal distribution, we compute the median for each wind-speed/wind-direction bin. For each wind-speed bin, we fit the resulting curve of median u_x values with the following function

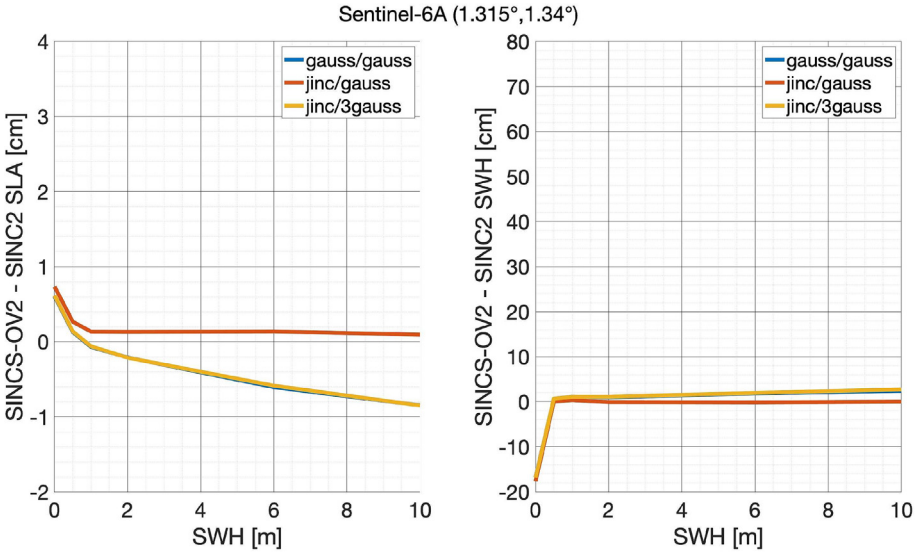

Fig. 8. Sentinel-6A mean retracking difference between SINCS-OV2 ZSK and SINC2 ZSK. Left: SLA. Right: SWH.

$$\tilde{u}_x(U_{10}, \varphi_w) = A_{u_x}(U_{10}) \cos(\varphi_w) + b_{u_x}(U_{10}) \tag{16}$$

where A_{u_x} and b_{u_x} are estimated parameters that describe the amplitude of the directional term and a mean offset.

For SLA we examine the differences between SINCS-OV2 ZSK and SINC2 ZSK as functions of the ERA5 SWH and ERA5 u_x. The latter is not a parameter in ERA5, but can approximately be computed from wind speed and wind direction with respect to the satellite track by (Buchhaupt et al., 2023)

$$u_x \propto \sqrt{U_{10}} \cos(\varphi_w) \tag{17}$$

Here we use edges of $H_s = \{0m, 0.25m, \ldots, 10m\}$ and $u_x = \{-12\ \mathrm{m/s}, -11.9\ \mathrm{m/s}, \ldots, 12\ \mathrm{m/s}\}$ when providing SLA difference histograms. E.g. we compute the histogram for all values between $H_s \in [0m, 0.25m]$, then between $H_s \in [0.25m, 0.5m]$, and so on. In the final step all histograms are normalized such that the one with the highest number of points has a maximum of one.

5.1. Sentinel-3A Global Analysis of Cycles 72 to 76

Fig. 9 shows the u_x fitting parameters with respect to the ERA5 wind speed while a Gaussian antenna pattern was

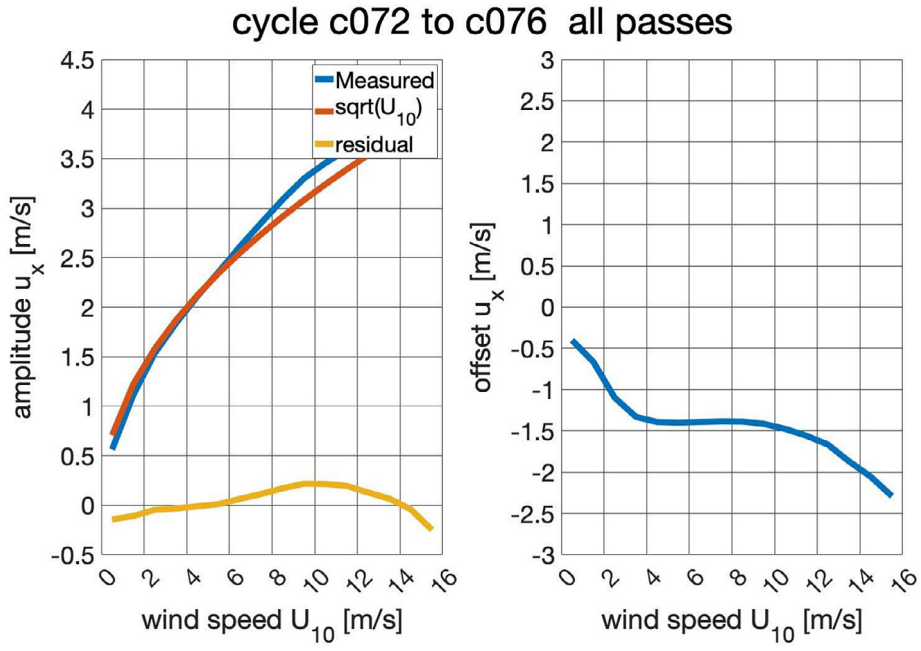

Fig. 9. The Sentinel-3A Gaussian antenna pattern u_x fitting parameters. No atmospheric refraction added.

assumed in the retracking. While the amplitude shows a very similar result as shown for Sentinel-6A in Buchhaupt et al. (2023) and can be approximated by a square root function, the offset parameter shows a trend with respect to ERA5 U_{10}. Results for $U_{10} < 3\,\mathrm{m/s}$ show a different pattern but as $U_{10} = 3\,\mathrm{m/s}$ corresponds to $H_s = 0.25m$ and altimetry results at very low sea states are usually not that accurate. The pattern for higher wind speeds is comparable to the simulation results presented in this study. If a sum of three Gaussian antenna pattern is used (see Fig. 10) in the retracking then the u_x offsets show that for wind speeds of $U_{10} > 3\,\mathrm{m/s}$ are below $0.25\,\mathrm{m/s}$ and therefore comparable to the simulations which show that using the correct antenna pattern leads to bias free u_x estimates. Amplitudes are identical to Fig. 9. Overall the sum of three Gaussian approximation improved the u_x fitting parameter. With a Gaussian antenna pattern used in the retracking SLA differences between SAR SINCS-OV2 ZSK and pseudo-LRM SINC2 ZSK show no significant u_x relationship, but a SWH dependency of up to $1.2\,cm$ is observable with a similar pattern as observed in the simulations (see Fig. 5). (see Fig. 11).

Fig. 12 - showing the results with a sum of three Gaussian approximation used in the retracker - shows no significant u_x dependencies. On the other hand, the sum of three Gaussian retracking results show significantly lower SWH dependencies of SLA differences. Differences are below $4mm$ with no clear SWH trend, besides for SWH of less

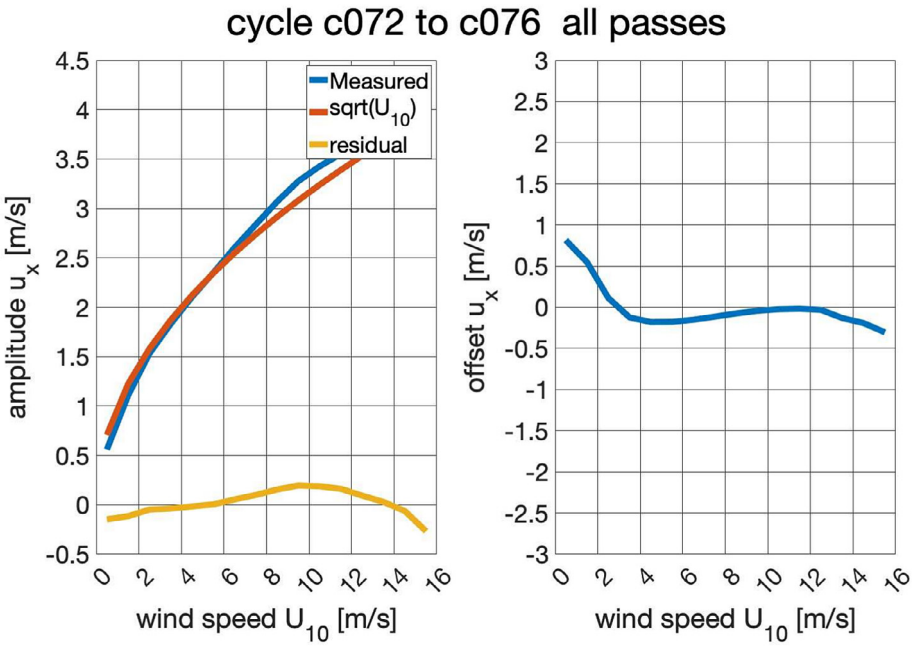

Fig. 10. The Sentinel-3A sum of three Gaussian antenna pattern u_x fitting parameters. No atmospheric refraction added.

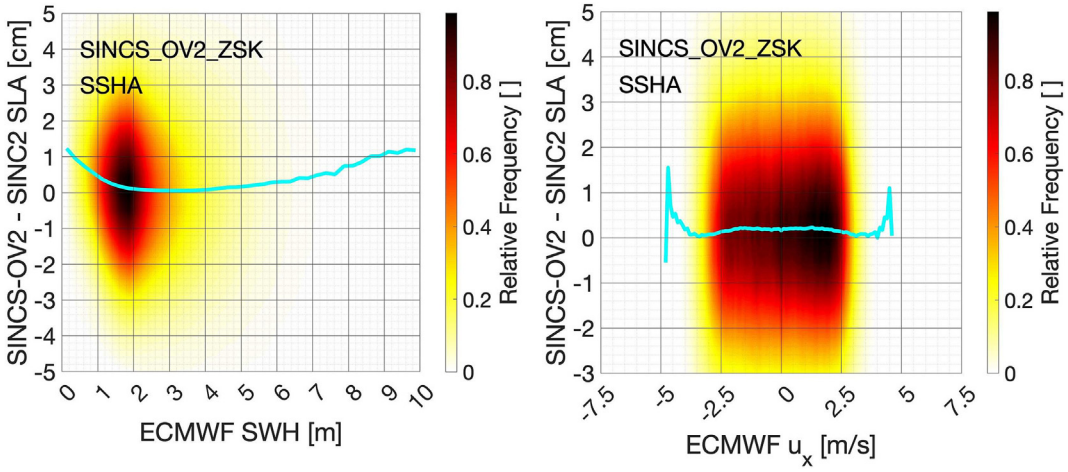

Fig. 11. The Sentinel-3A Gaussian antenna pattern retracking SLA differences between pseudo-LRM and SAR.

than two meter. The latter were observable in the simulations as well. Even so the sum of three Gaussian approximation improves the SLA consistency between SAR and pseudo-LRM, remaining differences of below 4*mm* are still unclear and need further investigations.

5.2. Sentinel-6A Global Analysis of Cycles 17 to 42

For Sentinel-6A we focus here on the sum of three Gaussian approximation results. The Gaussian antenna pattern results were already discussed in Buchhaupt et al. (2023). Fig. 13 shows for the amplitudes of the u_x fits the same results as for Sentinel-3A. As opposed to Buchhaupt et al. (2023, Fig. 8) the offsets show no trend but a mean of about 0.2 m/s. However, it is important to note that we applied the atmospheric refraction correction (about 2.08 m/s dependent on air pressure and water content) - presented in Buchhaupt et al. (2023) - to obtain this result. Since this effect was not observable for Sentinel-3A we are no longer sure that whether this effect is actually present, or whether some other issue is causing these offsets. The SLA differences between SAR SINCS-OV2 ZSK and pseudo-LRM SINC2 ZSK are below two millimeter for SWH of two meter or higher showing no significant trend, which indicate that the sum of three Gaussian in combination with $\theta_{3dBx} = 1.315^{\circ}$ yield consistent SLAs. Overall the sum of three Gaussian approximation works well for Sentinel-3A and Sentinel-6A. It can be concluded

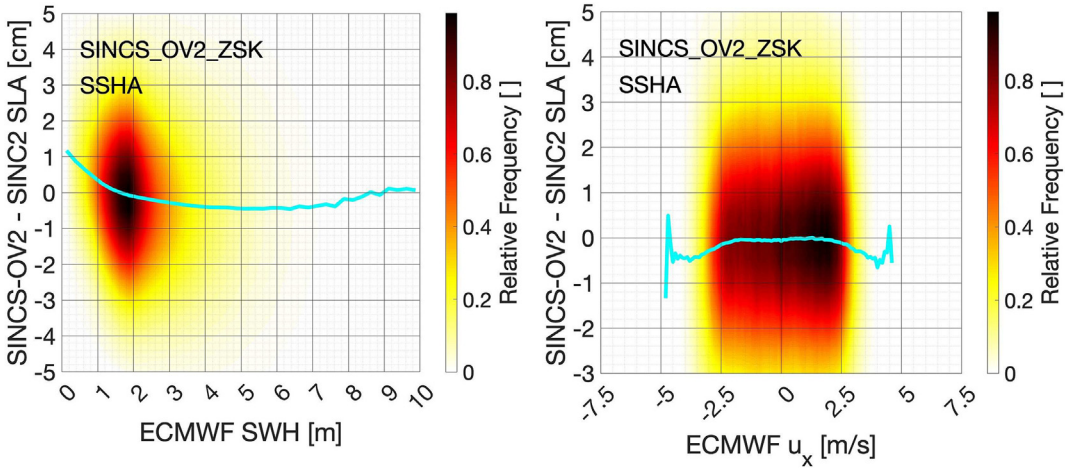

Fig. 12. The Sentinel-3A sum of three Gaussian antenna pattern retracking SLA differences between pseudo-LRM and SAR.

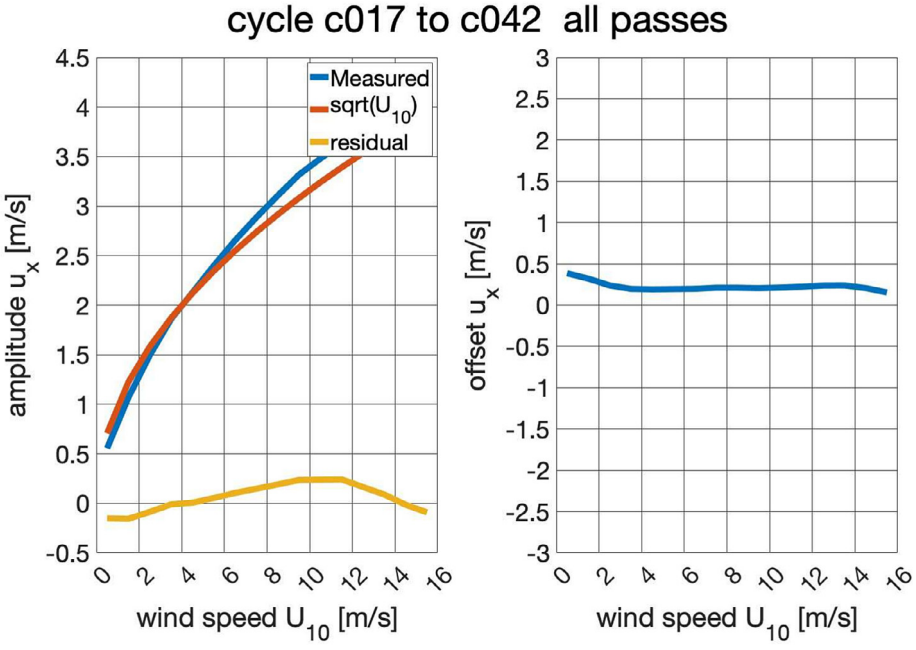

Fig. 13. The Sentinel-6A sum of three Gaussian antenna pattern u_x fitting parameters. Atmospheric refraction added.

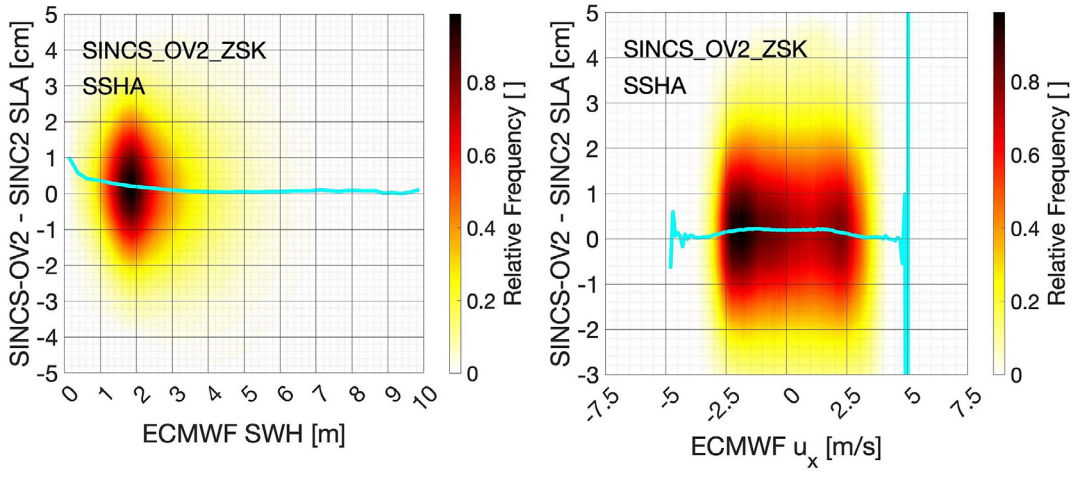

Fig. 14. The Sentinel-6A sum of three Gaussian antenna pattern retracking SLA differences between pseudo-LRM and SAR.

that the sum of three Gaussian approximation improves the u_x and SLA accuracy. However, in Buchhaupt et al. (2023) an atmospheric refraction effect was used to correct Sentinel-6A u_x estimates. This was not necessary here, which raises the question whether an atmospheric reflection correction is needed for Sentinel-3A or if something else is amiss.. We will investigate this remaining inconsistency in a further study. (see Fig. 14).

6. Conclusions

In this study, we introduce a new approach - called sum of three Gaussian approximation - to improve the representation of radar altimetry antenna characteristics, which provides SSH and SWH estimates with very good agreement, with respect to pseudo-LRM results.

We performed Monte Carlo runs to verify that the newly presented retracker approach provides bias-free estimates and showed that not considering a realistic antenna characterization in the retracking leads to significant SLA biases up to several centimeters and u_x up to $-3\frac{m}{s}$. On the other hand, SWH and the standard deviation of vertical wave-particle velocities σ_v are less affected by biases in the order of a few percentage points. By introducing the sum of three Gaussian approximation in the retracking we managed to eliminate almost all of the discrepancies between pseudo-LRM and SAR altimetry retracking results.

Additionally, we performed a half year global processing campaign of Sentinel-3A and Sentinel-6A data, which showed that the sum of three Gaussian approximation further improves the SAR and pseudo-LRM consistency. Additionally, the u_x offsets could be improved as well as they no longer show a trend with respect to wind speed. We could show that the Sentinel-6A along-track antenna beam width should be considered to be $\theta_{3dBx} = 1.315°$ compared to the value used in the processing of operational datasets of $\theta_{3dBx} = 1.34°$.

This study is also of concern for Ka-band altimeter missions like Satellite with ARgos and ALtiKa (SARAL) (Gac et al., 2015) and the upcoming Copernicus Polar Ice and Snow Topography Altimeter (CRISTAL) mission. Due to their small antenna beam width (compared to Ku-band altimeters), the Gaussian approximation of the antenna pattern typically considered in waveform models is no longer valid, requiring appropriate corrections to ensure accurate estimates. Implementing the approach developed in this study potentially provides unbiased estimates.

In further studies, we plan to perform an in situ validation campaign including tide-gauges and buoys to reinforce our findings. An investigation of remaining discrepancies between Sentinel-3A and Sentinel-6A with respect to the effect of atmospheric refraction on u_x needs to be performed as well. Since swell waves were not considered in this and previous studies we plan to investigate effects of those waves on retracker outputs as well.

Declaration of Competing Interest

The authors declare that they have no known competing financial interests or personal relationships that could have appeared to influence the work reported in this paper.

Acknowledgment

This research was supported by the NOAA component of the NASA-NOAA Joint program announced in NRA NNH20ZDA001N-OSTST: Ocean Surface Topography Science Team; Project/Proposal title: ”Towards an Improved Reconciliation of High- and Low-Resolution Ocean Altimeter Measurements Under Changing Surface Wave Structure Conditions”. It was also supported NOAA grants NA24NESX432C0001 and NA19NES4320002 (Cooperative Institute for Satellite Earth System Studies - CISESS) at the University of Maryland/ESSIC.

Appendix A. Simulation of Reduced and Unfocused SAR Signals

In this section we provide an overview about the simulations performed for Section 4 for each H_s and φ_w defined in Section 3. For unfocused SAR 10,000 and for pseudo-LRM 500,000 runs are performed for each H_s/φ_w realization. However, for pseudoLRM less simulations would most likely be sufficient as well, but since they are commutable very fast we chose a bigger number than necessary.

Each SAR stack and waveform simulation is conducted using the following steps:

1. Compute a noise-free numerical SAR DDM according to Eq. 10 and apply the slant range correction for current H_s/φ_wrealization with amplitude A and thermal noise of $t_n = \frac{A}{1000}$.
2. Add exponentially distributed noise to the SAR DDM for stack retracking. Additionally apply the ZSK transform (Buchhaupt, 2019) (Eq. (7.1)) to the resulting noisy DDM. Repeat this step N_b times.
3. Average all corresponding signals to get the retracker input.
4. Retrack - with $\mu = 0$to consider linear waves in the simulation - the SAR DDM with SINCS-OV2 ZSK.
5. Repeat steps two to four for each H_s/φ_w realization $9,999$ times to retrieve mean offsets with a high SNR.

For pseudo-LRM this simulation of realistic noise is not that easy as the effective number of looks is not constant over the whole waveform (Egido and Smith, 2019). To get a good approximation we define the effective number of looks here as the variance ratio between two Gamma distributed random variables. One with a shape parameter of one and the other with a shape parameter of $L_{eff,k}$. For both distributions the expected value is P_k, which shall describe the power of the pseudo-LRM waveform in sample k.

$$L_{eff,k} = \frac{Var[X_1 \sim \Gamma(1, P_k)]}{Var\left[X_2 \sim \Gamma\left(L_{eff}, \frac{P_k}{L_{eff}}\right)\right]} \tag{A.1}$$

in which e.g. $(1, P_k)$ means that X_1 is Gamma distributed with a shape parameter of one and a scale parameter of P_k.

Using the relationship between a SAR DDM (no slant range correction applied) P_{kl} and a pseudo-LRM waveform $P_k = \sum_{l=1}^{L} P_{k,l}$- with L the number of Doppler beams in the DDM - the effective number of looks can be determined from a DDM as

$$L_{eff,k} = \frac{\left(\sum_{l=1}^{L} P_{k,l}\right)^2}{\sum_{l=1}^{L} P_{k,l}^2} \frac{N_b}{O_x} \tag{A.2}$$

This requires uncorrelated Doppler beams in the DDM, which was investigated by Egido et al. (2021) showing that the correlation length for ocean surfaces observed by an altimeter in SAR mode are much smaller than the typical along-track resolution. Therefore, the approach chosen in this study should deliver a realistic noise representation within pseudo-LRM waveforms. The factor N_b/O_xin Eq. A.2 considers that N_b number of uncorrelated bursts are used to generate a 20-Hz waveform and that DDMs are over sampled by a factor of O_x, which would potentially lead to $O_x$as many effective number of looks than pulses per burst. A potentially more sophisticated way of computing the effective number of looks is presented in Wingham et al. (2018), which derives an analytical solution based on the power covariance function.

It is important to note that if a thermal noise shall be applied to the DDM which shall result into an e.g. one percent thermal noise in the pseudo-LRM waveform then the thermal noise applied to the whole DDM needs to be $t_{n,DDM} = t_{n,wvf}/L$. Fig. A.15 shows an example for a Sentinel-3A pseudo-LRM waveform with a SWH of two meter and a one percent thermal noise. Each pseudo-LRM waveform simulation is conducted using the following steps:

1. Compute a noise-free numerical SAR DDM according to Eq. 10. Do not apply the slant range correction. Additionally compute numerical pseudo-LRM waveform according to Eq. 11 for current $H_s$realization with amplitude A and thermal noise of $t_n = \frac{A}{1000}$.
2. Compute the effective number of looks $L_{eff,k}$ according to Eq. A.2 using the SAR DDM computed in step 1.
3. Simulate $L_{eff,k}$ exponentially distributed power values for each pseudo-LRM waveform sample.
4. Apply the ZSK power transform to each value computed in the previous step and average for each sample k over all $L_{eff,k}$ values.
5. Retrack - with $\mu = 0$to consider linear waves in the simulation - the pseudo-LRM multi looked waveform with SINC2 ZSK.
6. Repeat steps two to five for each $H_s$realization $499,999$times to retrieve mean offsets with a high SNR.

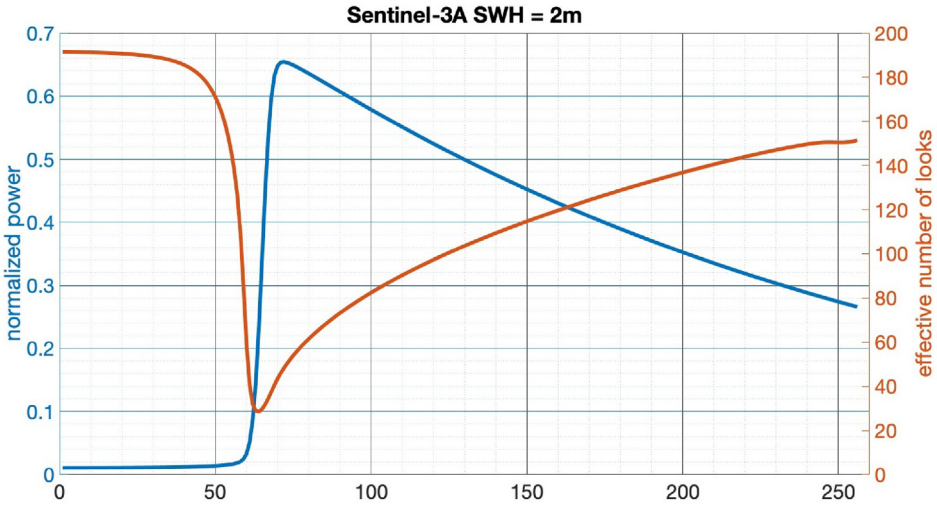

Fig. A.15 Effective number of looks for a Sentinel-3A reduced SAR waveform with a SWH of two meter and thermal noise of one percent of the maximum waveform power.

References

Amarouche, L., Thibaut, P., Zanife, O.Z., Dumont, J.-P., Vincent, P., Steunou, N., 2004. Improving the Jason-1 Ground Retracking to Better Account for Attitude Effects. Mar. Geodesy 27 (1–2), 171–197.

Brown, G., 1977. The average impulse response of a rough surface and its applications. IEEE Trans. Antennas Propag. 25 (1), 67–74.

Brown, G.S. (1975), Reduced backscattering cross section (σ^0) data from the Skylab S-193 radar altimeter, Technical report, NASA-CR-141401.

Buchhaupt, C., 2019. Model Improvement for SAR Altimetry PhD thesis. Technische Universität, Darmstadt.

Buchhaupt, C., Egido, A., Smith, W.H., Fenoglio, L., 2023. Conditional sea surface statistics and their impact on geophysical sea surface parameters retrieved from sar altimetry signals. Adv. Space Res.

Buchhaupt, C., Fenoglio-Marc, L., Dinardo, S., Scharroo, R., Becker, M., 2018. A fast convolution based waveform model for conventional and unfocused sar altimetry. Adv. Space Res. 62 (6), 1445–1463, The CryoSat Satellite Altimetry Mission: Eight Years of Scientific Exploitation.

Buchhaupt, C.K., Egido, A., Vandemark, D., Smith, W.H.F., Fenoglio, L., Leuliette, E., 2023. Towards the mitigation of discrepancies in sea surface parameters estimated from low- and high-resolution satellite altimetry. Remote Sensing 15 (17).

Chelton, D.B., Walsh, E.J., MacArthur, J.L., 1989. Pulse compression and sea level tracking in satellite altimetry. Journal of Atmospheric and Oceanic Technology 6, 407–438.

Dinardo, S., Maraldi, C., Daguze, J.-A., Amraoui, S., Boy, F., Moreau, T., Fornari, M., Cullen, R., Picot, N., 2022. Sentinel-6 MF Poseidon-4 Radar Altimeter In-Flight Calibration and Performances Monitoring. IEEE Trans. Geosci. Remote Sens. 60, 1–16.

Donlon, C., Berruti, B., Buongiorno, A., Ferreira, M.-H., Féménias, P., Frerick, J., Goryl, P., Klein, U., Laur, H., Mavrocordatos, C., Nieke, J., Rebhan, H., Seitz, B., Stroede, J., Sciarra, R., 2012. The global monitoring for environment and security (gmes) sentinel-3 mission. Remote Sens. Environ. 120, 37–57.

Donlon, C.J., Cullen, R., Giulicchi, L., Vuilleumier, P., Francis, C.R., Kuschnerus, M., Simpson, W., Bouridah, A., Caleno, M., Bertoni, R., Rancaño, J., Pourier, E., Hyslop, A., Mulcahy, J., Knockaert, R., Hunter, C., Webb, A., Fornari, M., Vaze, P., Brown, S., Willis, J., Desai, S., Desjonqueres, J.-D., Scharroo, R., Martin-Puig, C., Leuliette, E., Egido, A., Smith, W.H., Bonnefond, P., Le Gac, S., Picot, N., Tavernier, G., 2021. The copernicus sentinel-6 mission: Enhanced continuity of satellite sea level measurements from space. Remote Sens. Environ. 258, 112395.

Egido, A., Dinardo, S. & Ray, C. (2021), 'The case for increasing the posting rate in delay/doppler altimeters', Advances in Space Research 68(2), 930–936. 25 Years of Progress in Radar Altimetry.

Egido, A., Smith, W.H.F., 2016. Fully-Focused SAR Altimetry for Oceanographic Applications. In: AGU Fall Meeting Abstracts.

Egido, A., Smith, W.H.F., 2019. Pulse-to-pulse correlation effects in high prf low-resolution mode altimeters. IEEE Trans. Geosci. Remote Sens. 57 (5), 2610–2617.

Kleinherenbrink, M., Naeije, M., Slobbe, C., Egido, A., Smith, W., 2020. The performance of Cryosat-2 fully-focussed SAR for inland water-level estimation. Remote Sens. Environ. 237, 111589.

Le Gac, S., Poisson, J.-C., Piras, F., Thibaut, P., Boy, F., Valladeau, G., Guillot, A., Desjonqueres, J.-D., Picot, N., 2015. Impact of the antenna diagram approximation in conventional altimetry waveform processing: application to SARAL/AltiKa data. In: in '2015 Ocean Surface Topography Science Team Meeting'.

Moreau, T., Tran, N., Aublanc, J., Tison, C., Le Gac, S., Boy, F., 2018. Impact of long ocean waves on wave height retrieval from sar altimetry data. Adv. Space Res. 62 (6), 1434–1444, The CryoSat Satellite Altimetry Mission: Eight Years of Scientific Exploitation.

Pierson Jr., W.J., Moskowitz, L., 1964. A proposed spectral form for fully developed wind seas based on the similarity theory of S. A. Kitaigorodskii. Journal of Geophysical Research (1896–1977) 69 (24), 5181–5190.

Raney, R., 1980. SAR response to partially coherent phenomena. IEEE Trans. Antennas Propag. 28 (6), 777–787.

Ray, C., Martin-Puig, C., Clarizia, M.P., Ruffini, G., Dinardo, S., Gommenginger, C., Benveniste, J., 2015. SAR Altimeter Backscattered Waveform Model. IEEE Trans. Geosci. Remote Sens. 53, 911–919.

Raynal, M., Cadier, E., Labroue, S., Moreau, T., Féménias, P., Boy, F., Picot, N., Scharroo, R. & Borde, F. (2019), Lessons learned from Sentinel SARM missions in preparation of Jason-CS. Ocean Surface Topography Science Team Meeting (OSTST) 2019, Chicago, IL.

Rieu, P., Moreau, T., Cadier, E., Raynal, M., Clerc, S., Donlon, C., Borde, F., Boy, F., Maraldi, C., 2021. Exploiting the sentinel-3 tandem phase dataset and azimuth oversampling to better characterize the

sensitivity of sar altimeter sea surface height to long ocean waves. Adv. Space Res. 67 (1), 253–265.

Scagliola, M., Recchia, L., Maestri, L. & Giudici, D. (2021), 'Evaluating the impact of range walk compensation in delay/Doppler processing over open ocean', Advances in Space Research 68(2), 937–946. 25 Years of Progress in Radar Altimetry.

Stutzman, W.L., Thiele, G.A., 2012. Antenna Theory and Design, 3rd Edition. Wiley.

Tayfun, M., 1986. On Narrow-Band Representation of Ocean Waves: 1. Theory. J. Geophys. Res. 91, 7743–7752.

Walsh, E.J., 1982. Pulse-to-pulse correlation in satellite radar altimeters. Radio Science 17, 786–800.

Wingham, D.J., Francis, C.R., Baker, S., Bouzinac, C., Brockley, D., Cullen, R., de Chateau-Thierry, P., Laxon, S.W., Mallow, U., Mavrocordatos, C., Phalippou, L., Ratier, G., Rey, L., Rostan, F., Viau, P., Wallis, D.W., 2006. CryoSat: A mission to determine the fluctuations in Earth's land and marine ice fields. Adv. Space Res. 37, 841–871.

Wingham, D.J., Giles, K.A., Galin, N., Cullen, R., Armitage, T.W.K., Smith, W.H.F., 2018. A semianalytical model of the synthetic aperture, interferometric radar altimeter mean echo, and echo cross-product and its statistical fluctuations. IEEE Trans. Geosci. Remote Sens. 56 (5), 2539–2553.

Wingham, D., Phalippou, L., Mavrocordatos, C., Wallis, D., 2004. The mean echo and echo cross product from a beamforming interferometric altimeter and their application to elevation measurement. IEEE Trans. Geosci. Remote Sens. 42 (10), 2305–2323.